

# Three-dimensional simulations of rotationally-induced line variability from a Classical T Tauri star with a misaligned magnetic dipole

Ryuichi Kurosawa<sup>1?</sup>, M. M. Romanova<sup>2</sup> and Tim J. Harries<sup>3</sup>

<sup>1</sup>*Department of Physics and Astronomy, University of Nevada Las Vegas, Box 454002, 4505 Maryland Pkwy, Las Vegas, NV 89154-4002, USA.*

<sup>2</sup>*Department of Astronomy, Cornell University, 410 Space Sciences Building, Ithaca, NY 14853-6801, USA.*

<sup>3</sup>*School of Physics, University of Exeter, Stocker Road, Exeter EX4 4QL, UK.*

Dates to be inserted

## ABSTRACT

We present three-dimensional (3-D) simulations of rotationally induced line variability arising from complex circumstellar environment of classical T Tauri stars (CTTS) using the results of the 3-D magnetohydrodynamic (MHD) simulations of Romanova et al., who considered accretion onto a CTTS with a misaligned dipole magnetic axis with respect to the rotational axis. The density, velocity and temperature structures of the MHD simulations are mapped on to the radiative transfer grid, and corresponding line source function and the observed profiles of neutral hydrogen lines (H  $\gamma$ , Pa  $\gamma$  and Br  $\gamma$ ) are computed using the Sobolev escape probability method. We study the dependency of line variability on inclination angles ( $i$ ) and magnetic axis misalignment angles ( $\theta$ ). We find the line profiles are relatively insensitive to the details of the temperature structure of accretion funnels, but are influenced more by the mean temperature of the flow and its geometry. By comparing our models with the Pa  $\gamma$  profiles of 42 CTTS observed by Folha & Emerson, we find that models with a smaller misalignment angle ( $\theta < 15^\circ$ ) are more consistent with the observations which show that majority of Pa  $\gamma$  are rather symmetric around the line centre. For a high inclination system with a small dipole misalignment angle ( $\theta < 15^\circ$ ), only one accretion funnel (on the upper hemisphere) is visible to an observer at any given rotational phase. This can cause an anti-correlation of the line equivalent width in the blue wing ( $v < 0$ ) and that in the red wing ( $v > 0$ ) over a half of a rotational period, and a positive correlation over other half. We find a good overall agreement of the line variability behaviour predicted by our model and those from observations.

**Key words:** stars: formation – stars: pre-main-sequence – radiative transfer – line: formation

## 1 INTRODUCTION

Classical T Tauri stars (CTTS) are thought to accrue material from their circumstellar discs via magnetospheric accretion (MA). In this paradigm, the magnetic field of the protostar truncates the disc at a range of radii about corotation, from where the material flows along the field lines and onto the photosphere. The kinetic power of the material is thermalized in shocks (e.g. Camenzind 1990; Koenigl 1991) and is observed as a blue continuum excess (e.g. Calvet & Gullbring 1998), while the hot material within the funnel flows emits strongly in permitted lines (e.g. Alencar & Basri 2000). Observational and theoretical aspects of the MA paradigm were recently reviewed by Bouvier et al. (2007a).

There is now widespread observational support for the MA

model: CTTS are observed to have kilogauss magnetic fields that are persistent over timescales of years (Johns-Krull et al. 1999; Symington et al. 2005b; Johns-Krull 2007); the line profiles of hydrogen are Doppler broadened to a width comparable with the stellar escape velocity and the line profiles often show an inverse P Cygni profile that arises when an accretion funnel is viewed against a hot spot (e.g. Edwards et al. 1994; Alencar & Basri 2000; Folha & Emerson 2001); time-dependent line profile studies indicate the line profiles are modulated on the stellar rotation period (e.g. Johns & Basri 1995; Bouvier et al. 2007b).

Radiative-transfer models based on the MA paradigm are broadly successful in predicting line profile strengths and morphologies. Initial models were based on a simple aligned-dipole geometry for the accretion flow, but incorporated increasingly sophisticated physics starting from a two-level atom approximation (Hartmann, Hewett & Calvet 1994), through a full statistical equilibrium calculation under the Sobolev approximation (SA) by

? E-mail: rk@physics.unlv.edu

Muzerolle, Calvet & Hartmann (1998a), and finally including SA plus an exact integration of the line profile (Muzerolle et al. 2001).

The overwhelming evidence for variability, both in the continuum excess and the lines, of the emission from CTTS has lead us to examine departures from axisymmetry in the accretion geometry. A crude ‘curtains of accretion’ model (Symington, Harries & Kurosawa 2005a) was able to approximate rather well to the observed variability, providing that the accretion curtains had to have a relatively large azimuthal extent. A similar, tailored model for SU Aur was also able to reproduce some of the observed variability characteristics (Kurosawa, Harries & Symington 2005).

The last few years has seen the publication of a series of papers dealing with the magnetohydrodynamical modelling of accretion onto CTTS (Romanova et al. 2002; Romanova et al. 2003; Romanova et al. 2004, hereafter R02, R03 and R04 respectively; Long, Romanova & Lovelace 2007). But how well do these MHD models agree with the observational data? The simplest test is to attempt to model continuum light curves from the hot spot distributions of the models, and such simulations can reproduce the wide variety of observed variability. In particular for models with small magnetic misalignment angles the accretion funnels may rotate faster or slower than the star (meaning that the hot spots are not at fixed on the stellar surface), this naturally leads to the quasi-periodic variability that is often observed (R04). Useful though such comparisons are, the line profiles themselves encode much more detailed information on the kinematics and geometry of the flow. The aim of this paper is to make a quantitative comparison between the MHD models and spectroscopic observations by computing line profiles based on the density and velocity structure of the MHD calculations.

Here we concentrate on three hydrogen transitions ( $H\alpha$ ,  $H\beta$ , and  $H\gamma$ ). The  $H\alpha$  profile, although the strongest and most widely observed optical line, is usually contaminated by outflow emission and absorption (e.g. Reipurth, Pedrosa & Lago 1996) and cannot be modelled by MA alone, instead requiring a hybrid code incorporating both accretion and outflow (e.g. Kurosawa, Harries & Symington 2006). The  $H\gamma$  line is a better proxy for accretion, and observationally the near-IR lines show a high frequency of inverse P Cygni morphology, indicating that they too are better probes of the accretion geometry (Folha & Emerson 2001).

In the following Section we describe the MHD model and the radiative-transfer model, and we give the results of our profile calculations in Section 3. We discuss our results in comparison with both earlier radiative-transfer models and observations in Section 4, and our conclusions are presented in Section 5.

## 2 MODELS

The basic model configuration of the central star is shown Fig. 1. Two important parameters in our models, the misalignment angle and the inclination angle  $i$  are also shown in the figure. The former is defined as the angle between the rotational axis of the star (the  $z$ -axis) and the magnetic axis (with the dipole moment  $\mu$ ), while the latter is defined as the angle between the rotational axis and the direction to an observer. The rotational axes of the disc and the star coincide. In the following, we will describe our MHD models, radiative transfer models, assumed temperature structure and the sources of continuum radiation.

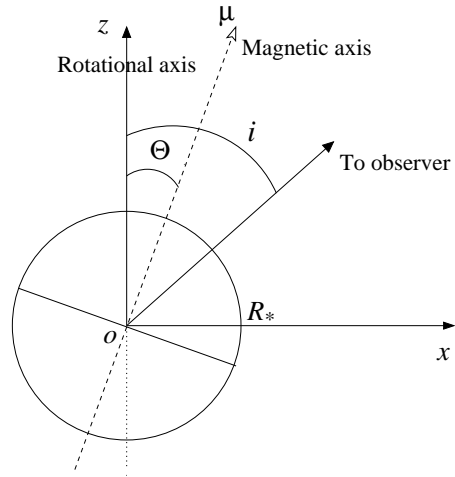


**Figure 1.** Basic model configuration. A star with its radius  $R_*$  is located at the origin ( $O$ ) of cartesian coordinate system ( $x, y, z$ ). The  $y$ -axis is into the paper. The rotational axis of the star coincides with  $z$ -axis. Its magnetic axis (with the magnetic moment  $\mu$ ) is inclined from the rotational axis by  $\Theta$ , causing precession of magnetic axis as the star rotates. This angle will be referred to as the misalignment angle. The inclination angle  $i$  is defined as the angle, measured from  $z$ -axis, to an observer located at infinity.

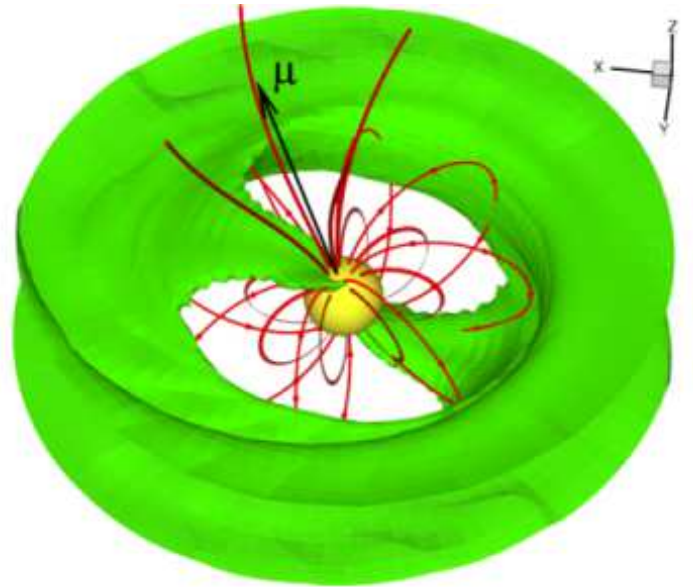


**Figure 2.** Example of three-dimensional simulations of MA flow for the magnetic axis misalignment angle  $\Theta = 15^\circ$ . The background shows the iso-surface for one of density levels, red lines show sample magnetic field lines, and the black arrow shows the direction of the magnetic moment of the star. The rotational axis coincides with  $z$ -axis.

### 2.1 MHD models

Three-dimensional MHD code and model used in this paper were developed and described earlier in Koldoba et al. (2002), R03, and R04. Here we briefly discuss the main aspects of the model and also describe new simulations runs.

We investigate matter flow around a rotating star with a misaligned dipole magnetic field. A star is surrounded with a dense cold accretion disk and a hot low-density corona above and below

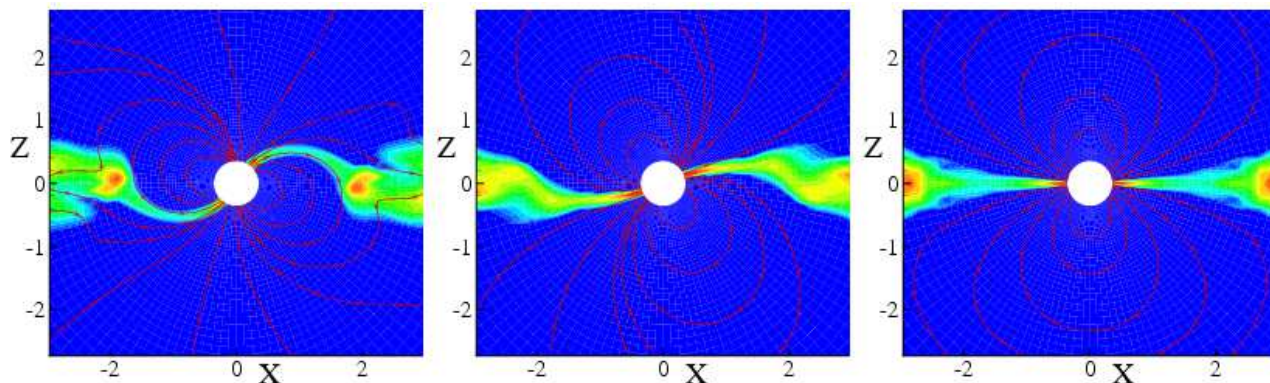


**Figure 3.** Slices of density distribution (background) and sample magnetic field lines for the simulations with the magnetic axis misalignment angle  $\theta = 15^\circ$  (left),  $60^\circ$  (centre) and  $90^\circ$  (right). The X-Z plane of slices coincides with the plane defined by the rotational axis and the magnetic axis (c.f. Fig 1). The red colour corresponds to the maximum of the density ( $\rho = 2 \rho_0$ ) while the dark blue colour to the minimum density ( $\rho = 0.003 \rho_0$ ) where  $\rho_0 = 4.9 \times 10^{12} \text{ g cm}^{-3}$ . The units of X and Z dimensions are in  $R_0 = 3.6 \times 10^{11} \text{ cm}$ . The accretion on to the surface occurs in two streams, and the latitudinal location where the gas impacts on the stellar surface decreases as  $\theta$  increases. These three density distributions (along with corresponding temperatures and velocities) will be used in the subsequent radiative transfer calculations.

it. To calculate matter flow we solve a full system of magnetohydrodynamic equations (in three dimensions) using a Godunov-type numerical code (see Koldoba et al. 2002; R03 and R04). Equations are written in the coordinate system rotating with the star. A viscosity term has been added to the code with viscosity coefficient proportional to the  $\eta$  parameter.

The boundary conditions used here are similar to those in R03 and R04. At the stellar surface, ‘free’ boundary conditions to the density and pressure are used. A star is treated as a perfect conductor so that the normal component of the magnetic field does not vary in time. There is however a ‘free’ condition to the azimuthal component of the magnetic field:  $\partial(RB_\phi)/\partial R = 0$  so that magnetic field lines have a ‘freedom’ to bend near the stellar surface. In the reference frame rotating with the star the flow velocity is adjusted such that to be parallel to the magnetic field  $B$  at  $R = R_0$  which corresponds to a frozen-in condition. Matter falls to the surface of the star supersonically and most of its energy is expected to be radiated in the shock wave close to the surface of the star (e.g. Camenzind 1990; Koenigl 1991; Calvet & Gullbring 1998). Evolution of the radiative shock wave above the surface of CTTSs has been considered in detail by Ustyugova et al. (2006). In this paper we suggest that most of kinetic energy of the flow is converted to radiation (see R04 and Section 2.4). At the outer boundary  $R = R_{\text{max}}$ , free boundary conditions are taken for all variables.

Numerical simulations have shown that the inner regions of the disk are disrupted by the magnetosphere of the star and matter flows to a star in two high-density funnels streams under some situations. Fig. 2 shows an example of such two-stream accretion for a system with the misalignment angle  $\theta = 15^\circ$  (see also R04; Kulkarni & Romanova 2005). The important parameters are the initial densities in the disk  $\rho_d$  and corona  $\rho_c$ , and the initial temperatures in the disk  $T_d$  and corona  $T_c$ . These values are determined at the fiducial point at the boundary between the disk and corona (at the inner radius of the disk). We took parameters  $\rho_c = 0.01 \rho_d$ ,  $T_d = 0.01 T_c$  and obtained supersonic funnel streams since the sound speed is relatively low,  $c_s \approx 0.1 v_K$ .

The funnel flow converges towards the star and temperature increases due to adiabatic heating. In reality, the temperature may decrease due to radiative cooling. To mimic the effect of the radiative cooling we performed most of these new runs at smaller

adiabatic index  $\gamma = 1.1$ . This is the main difference of the new runs compared to R04 runs. In addition, we increased the magnetic field of the star by a factor of two compared to R04. This led to larger magnetospheric gaps compared to R04.

We have adopted the following MHD input parameters from a typical CTTS. The mass and the radius of the star are assumed to be  $M = 0.8 M_\odot$  and  $R = 1.8 R_\odot$  respectively. The magnetic field at the surface of the star (at the equator) is assumed to be  $B = 4 \times 10^3 \text{ G}$ . The size of the simulation region corresponds to  $R_{\text{max}} = 40 R_0 = 0.34 \text{ AU}$ . The unit of time used in the model is  $P = P_0 = 1.38 \text{ d}$  which corresponds to a period of Keplerian rotation at  $R = R_0 = 3.6 \times 10^{11} \text{ cm}$  which is the unit distance used in Fig. 3. The star rotates with period  $P = 3.9 \text{ d}$  which corresponds to many CTTSs (e.g. Herbst et al. 2002). The accretion disc is stopped by the magnetosphere at the distance  $R_t = 1.6 R_0 = 5.8 \times 10^{11} \text{ cm}$ . This distance is slightly below the corotation radius of the star  $R_{\text{cor}} = 2 R_0 = 7.2 \times 10^{11} \text{ cm}$ . This situation approximately corresponds to the rotational equilibrium state in which a star does not gain or lose angular momentum on average (see Long et al. 2005). We consider the case with typical value of corona temperature and the disc density are set  $T_c = 4.5 \times 10^6 \text{ K}$  and  $\rho_0 = 4.9 \times 10^{12} \text{ g cm}^{-3}$  (e.g. Hartmann et al. 1998) respectively.

R03 and R04 showed that the geometry of the accretion stream strongly depends on  $\theta$ ; hence, we consider cases with a wide range of angles, specifically  $\theta = 15^\circ, 60^\circ$  and  $90^\circ$ . Fig. 3 shows the density slices of the 3-D simulations on the planes defined by the rotation axes and the misaligned magnetic axes. The figure shows the accretion occurs in two streams (as mentioned earlier), and the flows encounter the stellar surface near the magnetic poles (see R04 for their relative locations). We choose the time slices of these MHD simulations at which the flows are semi-steady and has a similar accretion rate ( $\dot{M}_{\text{acc}} \approx 2 \times 10^{-8} M_\odot \text{ yr}^{-1}$ ) for a comparison and for the radiative transfer models presented in the following sections. This mass-accretion rate chosen here is very similar to that of a typical CTTS seen in the observations (e.g. Gullbring et al. 1998; Calvet et al. 2004).

## 2.2 Radiative transfer model

The radiative transfer code TORUS (Harries 2000; Kurosawa et al. 2004; Kurosawa et al. 2005; Symington et al. 2005a; Kurosawa et al. 2006) was extended to incorporate the density, velocity and gas temperature structures from the 3-D MHD simulations of R04 mentioned above. The radiative transfer code uses the three-dimensional (3D) adaptive mesh refinement (AMR) grid, and it allows us an accurate mapping of the original MHD simulation data onto the radiative transfer grid. Although it is possible, we do not explore the line variability due to the time-dependent nature of the accretion in this paper. The aspect we investigate here is the variability due to the change in the viewing angles (of an observer) due to the rotational motion of a star and its magnetosphere. For this reason, we select outputs of MHD simulation which have (relatively) quiet stage, i.e. we choose the time stage of simulations which reached a (semi-) steady state.

We emphasise that the variability associated with the time-dependent nature of the flow (e.g. due to instabilities) is certainly worth pursuing in the future since it provides us an opportunity to study the kinematics of the accretion flow itself; hence, it would provide us an additional constraint on the geometry of the magnetosphere around CTTS. This is beyond the scope of this paper, but should be considered in a future work.

The basic steps for computing the line variability are as follows: (1) mapping of the MHD simulation output onto the radiative transfer grid, (2) the source function ( $S$ ) calculation and (3) the observed flux/profile calculation as a function of rotational phase. In the second step, we use the method of Klein & Castor (1978) (see also Rybicki & Hummer 1978; Hartmann et al. 1994) in which the Sobolev approximation method is applied. The population of the bound states of hydrogen are assumed to be in statistical equilibrium, and the gas to be in radiative equilibrium. Our hydrogen atom model consists of 14 bound states and a continuum. Readers are referred to Harries (2000) for details.

Monte Carlo radiative transfer (e.g. Hillier 1991), under the Sobolev approximation, is valid when (1) a large velocity gradient is present in the gas flow, and (2) the intrinsic line width is negligible compared to the Doppler broadening due to the bulk (macroscopic) motion of gas. In our earlier models (Harries 2000; Symington et al. 2005a), this method was adopted since these conditions are satisfied. However, as noted and demonstrated by Muzerolle et al. (2001), even with a moderate mass-accretion rate ( $10^{-7} M_{\odot} \text{ yr}^{-1}$ ), Stark broadening becomes important in the optically thick H line. In addition, H is most likely affected by the wind absorption and emission components (e.g. Edwards et al. 1994; Reipurth et al. 1996; Kurosawa et al. 2006), but the original MHD simulations (R03; R04) do not contain outflow/wind components. For these reasons we avoid modelling H, and concentrate on lines less likely to be affected by wind and Stark broadening, i.e. Pa (mainly), Br, and H in this paper.

When importing the MHD simulations results (Fig. 3) to the radiative transfer calculations, we have introduced a cut-off radius ( $r_{\text{max}} = 7.0 \times 10^{11} \text{ cm} = 5.5 R_{\odot}$ ) although the radial range of the MHD simulations extend much larger than this value. The cut-off radius corresponds  $X = 2.0$  in Fig. 3. This indicates that the puffed-up density structures in the disc seen in the MHD simulations are not included in the radiative transfer models, and the problems are rather focused on the accretion funnel parts. This is done to avoid the complications of adding dust opacity and finding dust temperature, and to avoid very high density and low temperature regions in which the source function calculation may have some dif-

ficulty. Beyond this cut-off radius, we simply inserted a ‘optically thick and geometrically thin disc’ which is essentially a geometrical disc with no thickness and with infinitely large opacity through which no radiation can penetrate. This type of disc was adopted to imitate the obscuration of the accretion funnels and stellar surface by a optically thick disc. Although we understand the importance of including the puffed-up regions of the disc and the dust for the line variability problems in very high inclination system, currently our model are not be able handle the regions correctly.

## 2.3 Temperature structure

The temperature structure of the magnetosphere used by Hartmann et al. (1994) is computed by assuming a volumetric heating rate which is proportional to  $r^{-3}$ , by solving the energy balance of the radiative cooling rate (see Table 1 in Hartmann, Avrett & Edwards 1982) and the heating rate. However, in this formulation, the normalisation is arbitrary, and it has to be determined from the multiple line fitting. On the other hand, Martin (1996) presented a self-consistent determination of the thermal structure of the inflowing gas, along the same dipole magnetic field geometry as in Hartmann et al. (1982), by solving the heat equation coupled to the rate equations for hydrogen. He found that main heat source is adiabatic compression due to the converging nature of the flow, and the major contributors to the cooling process are bremsstrahlung radiation and line emission from Ca II and Mg II ions. Muzerolle, Hartmann & Calvet (1998b) found that the line profile models computed according to the temperature structure of Martin (1996) do not agree with observations, unlike profiles based on the (less self-consistent) Hartmann et al. (1994) temperature distribution. It is clear that the temperature structure of the magnetosphere is still a large source of uncertainty in the accretion model, and this issue should certainly be investigated more carefully in the future.

In this paper we simply consider following three cases of the temperature structure of the flow: (1) Hartmann-like cooling/heating case, (2) adiabatic cooling/heating only case (directly from the MHD calculation), and (3) isothermal case. In case of (2), we find that the gas temperature from the MHD is in general too high (no radiative cooling); hence, we introduce a scaling factor  $s$  which is multiplied with the original temperature ( $T_{\text{MHD}}$ ) of the MHD simulations, i.e.  $T = s T_{\text{MHD}}$ . This is somewhat similar to an arbitrary normalisation constant introduced in (1). Note in all the models presented in this paper,  $s = 1.67 \times 10^{-2}$  and the MHD models results with the adiabatic index  $\gamma = 1.1$  (c.f. R04). Basic results of the dependency of line profiles will be presented in Section 3.2. In the following sections, (1) and (2) will be refer to as the HCH and ACH temperature structures, respectively.

## 2.4 The continuum sources

We adopt stellar parameters of a typical classical T Tauri star used by R04 for the central continuum source to be consistent with their MHD simulations, i.e. its stellar radius  $R = 1.8 R_{\odot}$  and its mass  $M = 0.8 M_{\odot}$  (see Section 2.1). Consequently, we adopt the effective temperature of the photosphere  $T_{\text{ph}} = 4000 \text{ K}$  and the surface gravity  $\log g = 3.5$  (cgs), and use the model atmosphere of Kurucz (1979) as the photospheric contribution to the continuum flux. The parameters are summarised in Table 1.

Additional continuum sources to be included are the hot spots formed by the infalling gas along the magnetic field on to the stellar

surface. As the gas approaches the surface, it decelerates in a strong shock, and is heated to  $\sim 10^6$  K. The X-ray radiation produced in the shock will be absorbed by the gas locally, and re-emitted as optical and UV light (Calvet & Gullbring 1998; Gullbring et al. 2000) – forming the high temperature regions on the stellar surface with which the magnetic field intersects. While Muzerolle et al. (2001), Symington et al. (2005a) and Kurosawa et al. (2006) used a single temperature model for hot spots assuming the free-falling kinetic energy is thermalized in the radiating layer, and is re-emitted as blackbody radiation, we adopt the multi-temperature hot spot model of R04 in which the temperature of the hot spots is also determined by conversion of kinetic energy plus internal energy of infalling gas to radiation energy (as a blackbody). They considered the position dependent matter flux crossing the inner boundary; hence, achieving a position dependent temperature of the hot spot, which can be written as

$$T_{hs} = \frac{\dot{m}_r}{2} \frac{1}{v^2 + w^2} \quad (1)$$

where  $p$ ,  $\rho$ ,  $v_r$  and  $v$  are the pressure, the density, the radial component of velocity and the speed of gas/plasma, respectively. Further more,  $k_B$  is the Stefan-Boltzmann constant, and  $w$  is the specific enthalpy of the gas:  $w = \frac{p}{\rho} + \frac{v^2}{2}$  (1). A typical temperature (area-weighted mean) of the hotspots is around 8000 K in our models.

We compare this temperature  $T_{hs}$  with the effective temperature of photosphere  $T_{ph}$  to determine the shape of the hot spots. If  $T_{hs} > T_{ph}$ , then the location on the stellar surface is flagged as hot. For the hot surface, the total continuum flux is the sum of the blackbody radiation with  $T_{hs}$  and the flux from the model photosphere mentioned above. The contribution from the inflow gas is ignored when  $T_{hs} < T_{ph}$ .

### 3 RESULTS

Using Pa  $\alpha$  as an example, the general characteristics of line variability computed by the radiative transfer model will be presented in this section. We present models with 5 different combinations of the misalignment angle  $\theta$  and inclination angle  $i$ , as summarised in Table 2. First, we present the continuum variability of our models. Second, we briefly discuss the dependency of the models on the temperature structures (c.f. Section 2.3). Third, we discuss the dependency on other main input parameters ( $i$  and  $\theta$ ). Fourth, we compare line profiles for different transitions (H  $\gamma$ , Pa  $\alpha$  and Br  $\gamma$ ). Finally, we will present line equivalent widths computed as a function of rotation phase. Unless specified otherwise, we adopt the stellar parameters in Table 1 for a central star. The mass-accretion rate ( $\dot{M}_{acc}$ ) and the inner radius ( $R_d$ ) of the accretion disc used in our models are also shown in the same table.

#### 3.1 Continuum Variability

Since the line variability is closely related with the continuum variability, we present the light curves predicated by the models before we present the line variability results. R04 also presented the light curves of the 3-D MHD simulations which are basically identical to ours. Their light curves were computed by using frequency-integrated flux and do not contain an optically thick disc which would obscure the stellar photosphere and accretion hot spots at high inclination angles. On the other hand, our model computes the light curves at a given wavelength, and contains an optically-thick

and geometrically thin disc. Fig. 4 shows the light curves computed at  $\lambda_c = 4800$  Å for all the models listed in Table 2.

Comparing the light curves from Models A, B and C which use the same MHD model ( $\theta = 15^\circ$  case), one can see the dependency on the inclination angle. Note that the hot spots are located about  $30^\circ$  from the poles of the rotational axis for these models (c.f. Figure 6; also see Fig. 7 of R04). The amplitude of the light curve oscillations increases as  $i$  increases up to  $i = 60^\circ$  (Model B). Although the models with  $i$  between  $0^\circ$  and  $60^\circ$  are not shown here, the same trend is observed in the additional models we have run. A similar trend was also observed by R04 — see their Fig. 10. As  $i$  becomes greater than  $60^\circ$ , the peak amplitude does not change greatly since a part of the second hot spot on the lower hemisphere becomes visible at higher inclinations.

The visibility of the second hot spots affects the shape of the light curve. In Model A and B, only one hot spot (on the upper hemisphere) is visible during the whole or parts of rotational phase; hence, their light curves exhibit a single peak in one rotational phase. On the other hand, two hot spots are visible in Models C, D and E (c.f. Figures 6 and 7). As a consequence, their light curves have two peaks in one rotational phase. Note that the Model C does not show a clear second peak, but the shape of the light curve is heavily affected by the presence of the second spot.

For the models with a fixed inclination angle but with different misalignment angles (Models B, D and E), the oscillation amplitudes are similar to each other except for Model E that has a large misalignment angle ( $90^\circ$ ). The shape of the hot spots in Model E is extremely elongated, and has almost a belt like shape located near the equatorial plane (c.f. Figure 7; also see Fig. 2 of R04). The gap between one edge of the ‘belt’ like structure to the next is  $\sim 40^\circ$ , causing a smaller peak-amplitude of oscillations.

The amplitude of the light curves ( $\Delta m = 0.4$ ) of Models B, C and D are comparable to that of AA Tau observed in V-band ( $\Delta V = 0.5$ ) by Bouvier et al. (2007b). This suggests that the continuum sources (Section 2.4) used in our models are quite reasonable.

#### 3.2 Dependency on temperatures structures

We examine how the different assumed temperature structures introduced in Section 2.3 affect the line profiles. As a demonstration, we compute Pa  $\alpha$  from a system viewed at  $i = 60^\circ$  and at the rotational phase  $\phi = 0.75$ , with a misalignment angle  $\theta = 15^\circ$  (Model B in Table 2; see also Figs. 2 and 3).

In particular, we will compare the profiles computed with the HCH, ACH temperature structures (c.f. Section 2.3), and an isothermal case ( $T_{iso} = 8000$  K). We choose normalisations/scalings of the temperature structures in HCH and ACH models such that their density-weighted mean temperatures ( $T_{mean}$ ) of the gas are comparable to that of the isothermal case ( $\sim 8000$  K).

The results are shown in Fig. 5. The profiles computed with the HCH and ACH are very similar to each other – they have similar flux in both wings, but the core flux of the HCH model is slightly larger than that of the ACH model. On the other hand, the isothermal model produces an inverse P-Cygni (IPC) profile with a shallower absorption wing. The difference is mainly caused by the warmer gas stream present in the outer part of the magnetosphere (where absorption occurs) compared to that of the HCH and ACH models. The core flux of the isothermal case is very similar to that of the HCH model. Overall, the profile shapes from all three temperature structures are very similar to each other. From this exercise, we find that the main physical conditions which de-



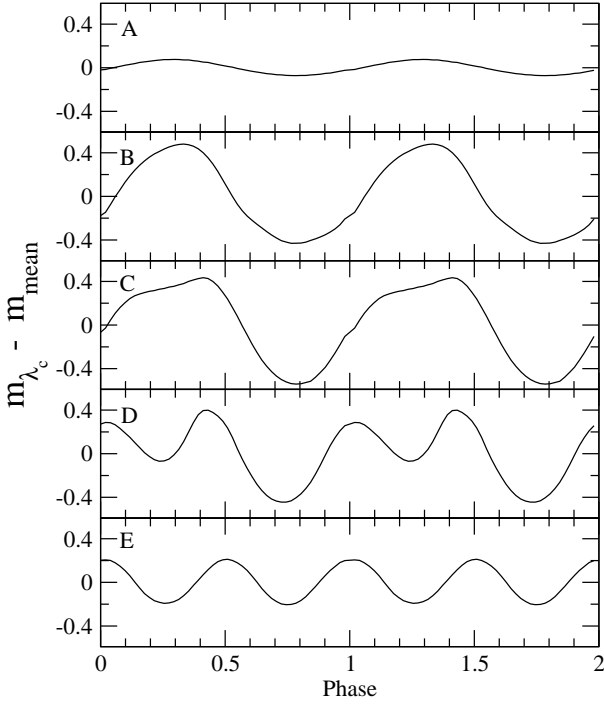


**Figure 4.** Continuum light curves for Models A to E (from top to bottom) at the wavelength  $\lambda_c = 4800 \text{ \AA}$  (near H $\gamma$ ). The vertical axis is scaled in pseudo-magnitude which is defined as  $m_{\lambda_c} = -\log_{2.51} F_{\lambda_c} + m_0$  where  $F_{\lambda_c}$  and  $m_0$  are the flux in cgs and the offset magnitude respectively. To avoid defining the arbitrary offset value, we have subtracted the mean magnitude  $m_{\text{mean}}$  (over entire rotational phases) from  $m_{\lambda_c}$ .

M	R	$T_e$	M–	$R_d$
M	R	(K)	$\text{yr}^{-1}$	R
0:8	1:8	4000	$2 \times 10^8$	8:6

**Table 1.** Reference Model Parameters

termines the profile shapes, *for a fixed mean temperature condition*, are the velocity field and the geometry of the funnel flows. In other words, as long as the mean temperature is similar, the difference in the temperature structure along the stream does not make a significant difference in line profiles at least at the temperature used here (8000 K). Since we find no large difference between the profiles from the HCH and ACH temperature structures, we adopt the latter (with  $T_{\text{mean}} = 8000\text{K}$ ) in the models presented in the following sections unless specified otherwise.

Model	A	B	C	D	E
Dipole offset,	15	15	15	60	90
Inclination, $i$	10	60	80	60	60

**Table 2.** A summary of the main model parameters

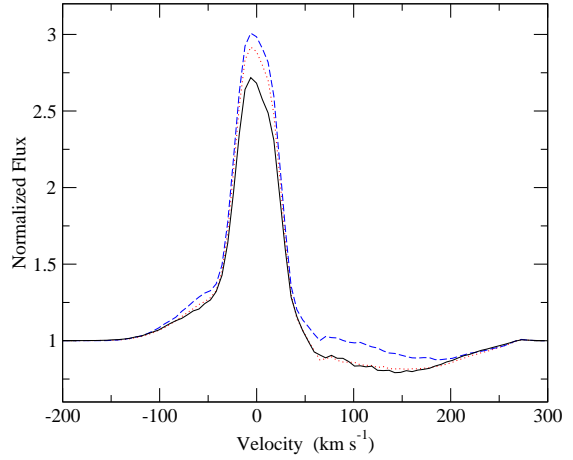


**Figure 5.** Comparison of Pa $\gamma$  with three different temperature structures of the accretion stream with  $\theta = 15^\circ$  and  $i = 60^\circ$  (Model B) at the rotational phase  $t = 0.75$ . Three cases considered here are: (1) the ACH model: the temperature structure from R04 (solid), (2) the HCH model: temperature structure from Hartmann et al. (1994) (dotted), and (3) an isothermal ( $T = 8000 \text{ K}$ ) case (dashed). The normalisation of the temperature structure scalings are chosen such that the mass-weighted mean temperature ( $T_{\text{mean}}$ ) of the flow is comparable to that of the isothermal case, i.e.  $T_{\text{mean}} = 8000 \text{ K}$ . Overall shapes of the profiles are very similar to each other, but the absorption in the red wing is slightly shallower for the isothermal case compared to the other two cases. The difference in the temperature structure in the accretion funnels does not make a significant difference in the profile shape as long as the mean temperature of the flows is similar.

### 3.3 Dependency on inclination $i$

Next we examine the dependency of the line variability on inclination angles using the MHD models with  $\theta = 15^\circ$ . Fig. 6 summarises the emission maps and profiles (Pa $\gamma$ ) for three different inclination angles  $i = 10^\circ$ ,  $60^\circ$ , and  $80^\circ$  (Models A, B, and C in Table 2 respectively), computed at four different rotational phases  $t = 0; 0.25; 0.5$  and  $1.0$ . The accretion onto the photosphere occurs along two streams (R04); creating two hot spots on the surface – one on each hemispheres. The hot spots are located about  $30^\circ$  from the rotational axis and have an ‘elongated kidney-bean’ shape (see also Fig. 2 in R04). For small inclination cases (e.g.  $i = 10^\circ$ , Model A), one spot is clearly visible at all rotational phases, but for higher inclinations, no spot is visible at certain rotational phases. The visibility of spots is very important for formation of the IPC profile and the variability of its absorption component; hence, the sizes and the location distributions of spots should be understood for a given model.

The good visibility of the hot spot for  $i = 10^\circ$  (Model A) results in the presence of the weak absorption in the red wing of the model at all rotational phases; however, the weakness of the absorption is caused by the unfavourable alignment of spot-funnel-observer line of sight. For  $i = 60^\circ$  (Model B) and  $80^\circ$  (Model C), the absorption feature in the red wing becomes most visible at the rotational phase when a spot is facing towards (i.e.  $t = 0.75$ ) the observer. The largest amount of red wing absorption occurs at the rotational phase at which a hot spot is facing the observer and when the spot-funnel-observer alignment is favourable e.g. for  $t = 0.75$  and  $i = 60^\circ$ .

The intensity maps show that most of the Pa $\gamma$  line flux contribution is from the gas in the funnels just above the hot spots (displayed in purple). For a high inclination case (e.g.  $i = 80^\circ$ ), the

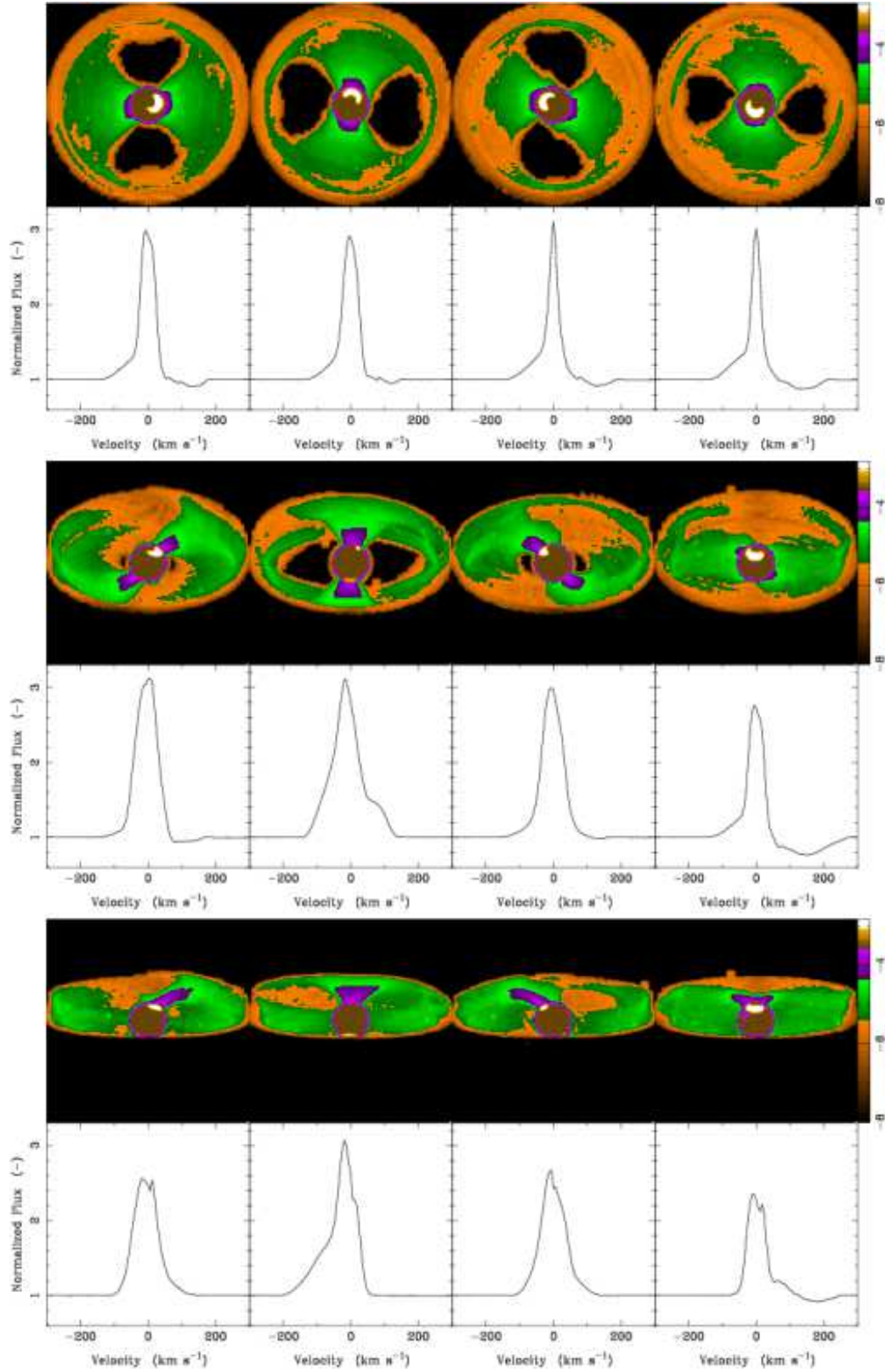


**Figure 6.** Pa model intensity maps and the corresponding profiles computed at rotational phases  $\tau = 0.0, 0.25, 0.5$  and  $0.75$  (from left to right) and for inclination angles  $i = 10^\circ, 60^\circ$ , and  $80^\circ$  (from top to bottom). The misalignment angle of the magnetic axis is fixed at  $\alpha = 15^\circ$  for all the models shown here. The intensity is shown in logarithmic scale with an arbitrary units. The physical dimension of the images are  $1.4 \times 10^{12}$  cm ( $\approx 11 R_\odot$ ) in both horizontal and vertical directions. The top, middle and bottom correspond to Model A, B and C in Table 2 respectively.

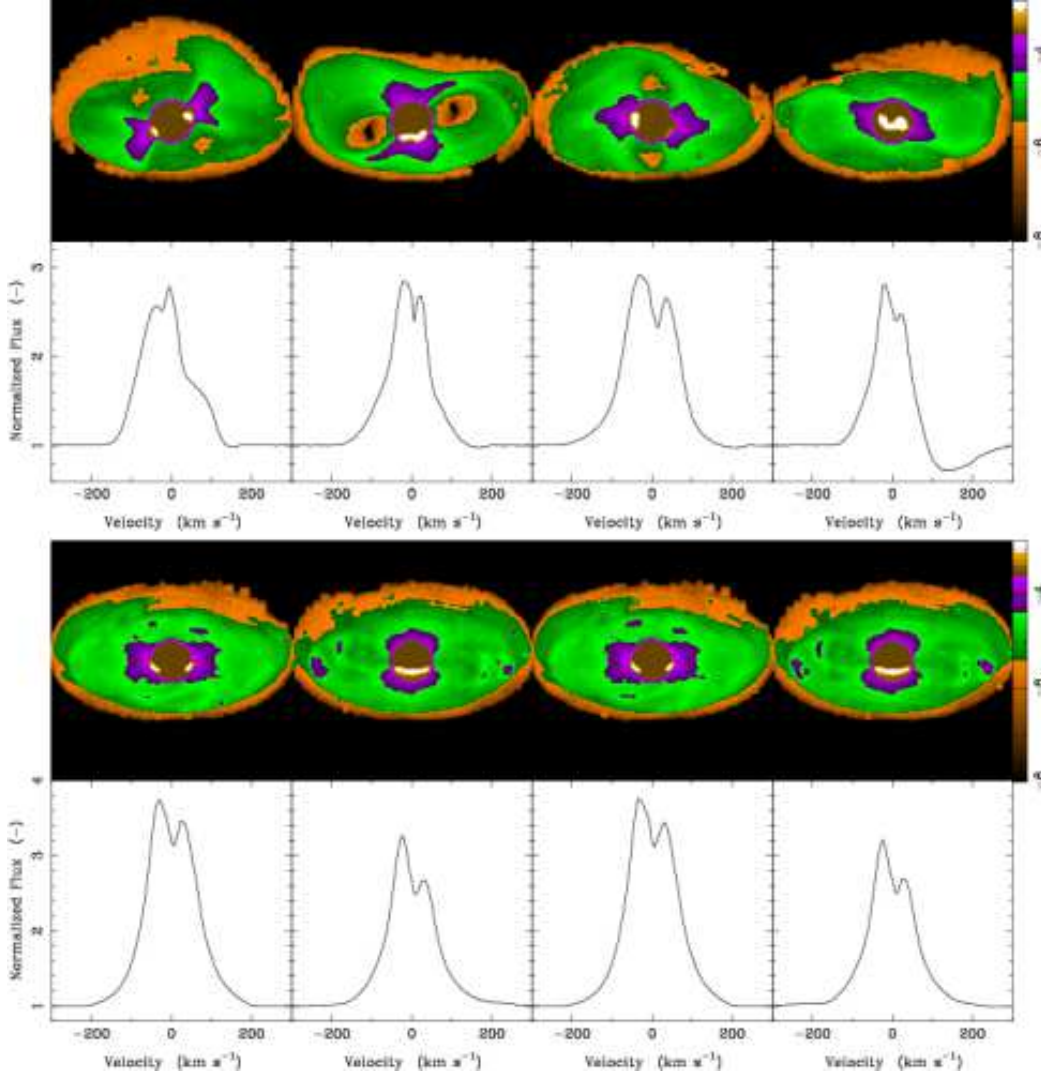


**Figure 7.** Same as in Fig. 6, but for Models D (upper panels) and E (lower panels) (c.f. Table 2).

presence of an accretion disc greatly affects the line profiles. For such cases, the line of sight to the accretion funnel located below the equatorial plane is obscured by the disc at all rotational phases. The blue-asymmetry (c.f. Folha & Emerson 2001) of the profile becomes largest at  $t = 0.25$  (for  $i = 80^\circ$ , Model C) as little gas is moving toward an observer at this phase. On contrary, a half rotation later ( $t = 0.75$ ), the profile does not become as asymmetric as the one at  $t = 0.25$  since the self-absorption of the photons in the stream significantly reduces the flux in the red wing.

The line variability behaviour of Models A, B and C are summarised in Fig. 8. The figure shows the mean spectra (phase averaged spectra), the quotient spectra (which are the original profiles divided by the mean spectra) as a function of rotational phase (in greyscale image), and the normalized variance spectrum (NVS), which is similar to the root-mean-square spectra (c.f. Johns & Basri 1995), for each model. The mean spectra of the three models are fairly symmetric about the line centre; however, a very weak but noticeable amount of absorption in the red wings can be seen in the spectra at all  $i$ . For  $i = 10^\circ$  and  $60^\circ$  cases (Models A and B), the flux level in their red wing becomes slightly below the continuum level, but the level remains above the continuum for the  $i = 80^\circ$

case (Model C). Although the line equivalent width of the mean spectra for  $i = 10^\circ$  is slightly smaller than that of  $i = 60^\circ$  and  $80^\circ$  cases, no significant difference is seen in three models. In addition to the quotient spectra in Fig. 8, the phase dependent spectra of each model are also shown in Fig. 9 as a different representation of the line variability.

The amount of the flux variability as a function of wavelength is summarised as the NVS. For  $i = 10^\circ$  (Model A), similar levels of variations are seen in the red and blue sides. The NVS is double-peaked, and is symmetric around the line centre. This variability pattern (NVS) is very similar to that of H $\alpha$  and H $\beta$  from the CTTS CW Hydra (K7Ve) presented by Alencar & Batalha (2002). The system has a low inclination angle ( $i = 18^\circ \pm 10^\circ$ , Alencar & Batalha 2002) which is consistent with our Model A ( $i = 10^\circ$ ). The variability patterns of the red and blue sides are also very similar to each other as seen in the grey scale image. As  $i$  increases, the symmetry breaks; the fraction of peak strength on the red to that on the blue becomes smaller. The peak levels the NVS (on the red side) for  $i = 60^\circ$  and  $80^\circ$  are similar ( $\sim 10$  per cent), but are about twice the size in the  $i = 10^\circ$  case.



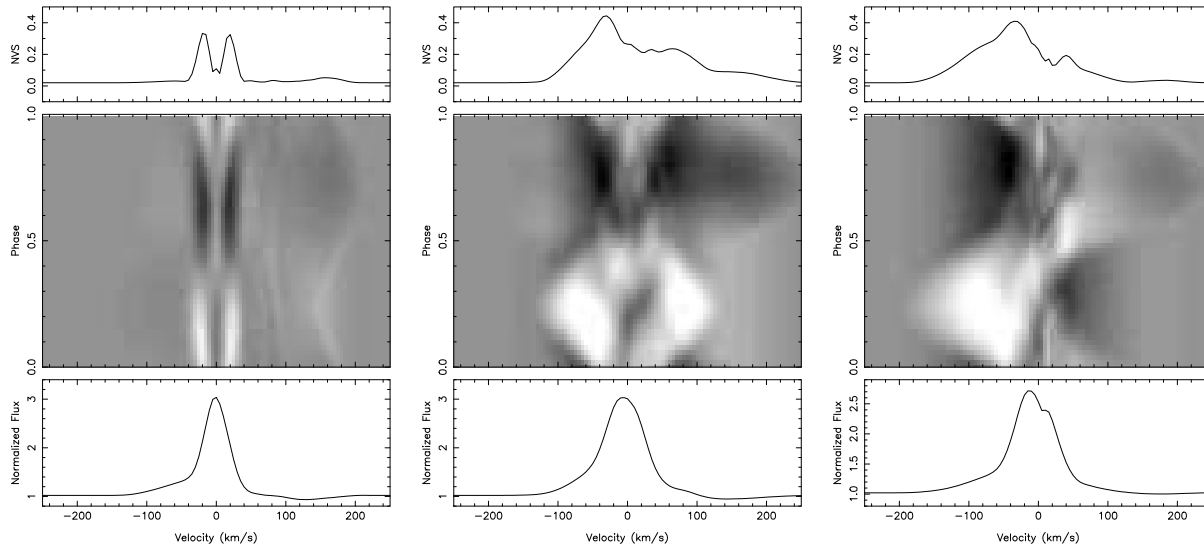


**Figure 8.** The summary of the Pa spectra computed for Model A (left), Model B (centre) and Model C (right) which are viewed with inclination angles ( $i$ ) of 10°, 60° and 80° respectively (c.f. Fig. 6). All three models have physically same accretion stream, i.e.  $\beta = 15^\circ$ . For each model, spectra were computed at 50 different rotational phases. In the bottom panels, the mean spectra of all rotational phases are shown. In the middle panels, the quotient spectra (each spectrum divided by the mean spectrum) are shown as greyscale images with increasing rotational phases in upward vertical direction. The greyscale image is scaled from 1:1 (white) to 0:9 (black). The normalized variance spectra NVS (Johns & Basri 1995) are shown in the top panels. The mean spectra for  $i = 10^\circ$  and  $60^\circ$  are almost symmetric about the line centre, but they do exhibit a very weak absorption in their red wings. The greyscale images shows that the red absorption are sometime stronger (black regions) and some time weaker (white regions) than the ones seen in the mean spectra. A little absorption in the red wing is seen for  $i = 80^\circ$  case. The ratio of the amount of the variability in red wing to that in blue wing decrease as  $i$  increases.

### 3.4 Dependency on misaligned angle

Next, we compare the models with three different misalignment angles:  $\beta = 15^\circ, 60^\circ$  and  $90^\circ$  (Models B, D and E respectively). The inclination angle  $i$  is fixed at  $60^\circ$  for these three models. Pa profiles at rotational phase  $t = 0, 0.25, 0.5$  and  $0.75$  along with the corresponding spatial intensity maps are shown in Figs. 6 (for Model B) and 7 (for Models D and E). Although the shapes of the funnel flows are different, the accretion still occurs in two streams for all these models, causing two hot spots on the stellar surface. The width of the stream becomes wider as  $\beta$  increases, and consequently the azimuthal extent of the hot spots also becomes wider. The latitudinal position of the hot spots becomes lower as the misalignment angle increases (c.f. Fig. 3). For  $\beta = 90^\circ$  case (Model E), the two wide and thin funnels are located almost on equatorial plane (c.f. Fig. 3), and so are the hot spots. See R04 for larger and clearer depiction of the hot spot geometries and their physical properties. Interestingly, similar equatorial flows and the shape of hot spots are found in a quadrupole magnetic field accretion model of Long et al. (2007) with a small misalignment angle.

The IPC profiles are found at  $t = 0.75$  for  $\beta = 15^\circ$  (Model B) and  $\beta = 60^\circ$  (Model D), but not for  $\beta = 90^\circ$  (Model E). The nearly equatorial accretion flows in Model D do not have a favourable spot-stream-observer line of sight which is essential for the formation of the IPC profile. The double-peaked profiles are seen for larger  $\beta$  models (Models D and E). The splitting of the peaks are caused by the rotational motion of the magnetosphere.

Figure 10 shows the summary of the line variability (Pa) for Models B, D and E. The mean line profile becomes wider as  $\beta$  increases. The separation of two peaks in the mean profile is largest for  $\beta = 90^\circ$ . The peak levels of the NVS are similar for all three models, but the location of the peak(s) is different. While the amount of variability is largest at the line centre for Model E

( $\beta = 90^\circ$ ), it is largest in the blue wing ( $v \approx 40 \text{ km s}^{-1}$ ) for Models B and D. We note that variability pattern seen in Model E resembles that of H $\gamma$  from the CTTS AA Tau observed by Bouvier et al. (2007b) although their inclination angle ( $i = 75^\circ$ ) is different from the model presented here ( $i = 60^\circ$ ). See also Fig. 9 for the summary of the phase dependent spectra.

### 3.5 Comparison of different lines

Once again using the models with  $\beta = 15^\circ$  (Models A, B and C) as examples, we demonstrate the difference in the line shapes among different hydrogen lines: Pa, Br and H $\gamma$ . The summary of the comparison spectra is shown in Figure 11. Although they differ in strength, the overall dependency of the line profile shape on the inclination angle is very similar in these three transitions. The relative line strength slightly decreases from H $\gamma$  to Pa then to Br. The line cores are narrower for higher inclination angle models. The strength of the blue wings are similar for  $i = 10^\circ$  and  $60^\circ$ , but much weaker in the higher inclination model  $i = 80^\circ$  since most of the flow moving toward an observer (blueshifted flows) is eclipsed by the stellar surface at a higher inclination (c.f. Fig. 6).

The line variability behaviour for each line computed at  $i = 60^\circ$  is summarised in Figure 12. All three lines show a very similar variability pattern in both the NVS spectra and the grey scale quotient spectral images. Interestingly, the peak level of NVS for H $\gamma$  is about 4 times larger than those of Pa and Br. The difference in the size of variability can be explained by a much larger spatial extent of the line emission regions for H $\gamma$  compared to Pa and Br.

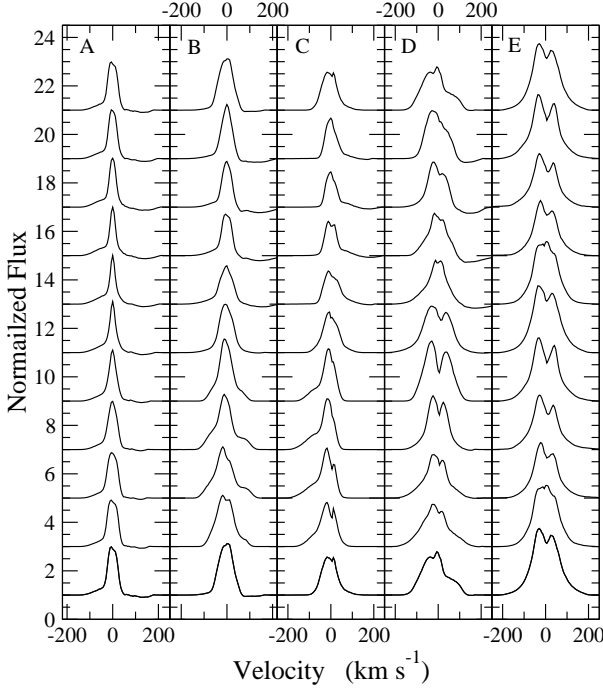


**Figure 9.** The time-series spectra of Pa  $\beta$  from Models A through E (from left to right,) are shown for 10 different rotational phase. From the top to the bottom the phase changes from 0 to 1. Each profile is separated by the rotational phase of  $\pm 0.1$ , and shifted upward by  $1.5$  as the rotational phase increases for clarity.

### 3.6 Line equivalent width

The phase dependency of the line EW (Pa  $\beta$ ) from each model in Table 2 is shown in Figure 13. We compute three different types of EWs: (1) by using all velocity bins in the model profile (from  $-500$  to  $500 \text{ km s}^{-1}$ ), (2) by using only negative velocity bins (the blue wing:  $-500$  to  $0 \text{ km s}^{-1}$ ), and (3) by using only positive velocity bins (the red wing:  $0$  to  $500 \text{ km s}^{-1}$ ). Similar methods are often used in time-series spectra observations (e.g. Johns & Basri 1995; Kurosawa et al. 2005) to examine the gas kinematics of the flow. Note that here we use the convention of the sign for the line EWs as negative when the flux is below the continuum and positive for vice versa.

For the model with  $\theta = 15^\circ$  and a mid to low inclination angle (i.e. Models A and B), the EW curves show only one minima (at phase  $\tau = 0.75$ ) in one rotational period. On the other hand, with the same physical model ( $\theta = 15^\circ$ ) but with a high inclination angle (i.e.  $i = 80^\circ$  as in Model C), the shapes of the EWs are affected by the presence of a second local minima at  $\tau = 0.25$ , especially in the red wing (positive velocity bins) EW curve which clearly shows two local minima in one rotational period. The local minima at  $\tau = 0.75$  is caused by the maximum continuum flux (c.f. Fig. 4) contribution from the hot spot in the upper hemisphere (c.f. Fig. 6). The second local minima at  $\tau = 0.25$  is caused by the combination of the following two reasons. First, at the high inclination, only one accretion arm is visible to an observer. Furthermore, at this rotational phase, the flow component which is moving away from the observer almost completely disappears because of the orientation of the remaining upper accretion arm (c.f. Fig. 6) hence causing the minimum flux in the red wing, which corresponds to the minimum EW of the red wing. Secondly, the visibility of the

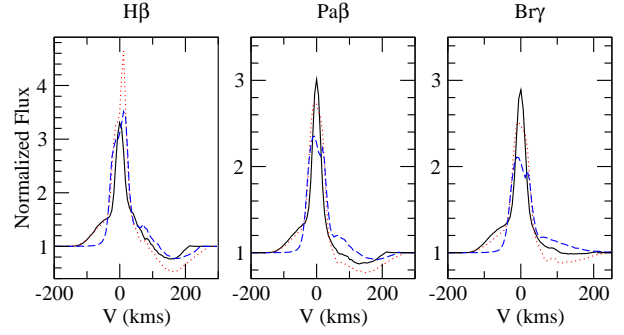


**Figure 11.** Comparison of H  $\beta$ , Pa  $\beta$  and Br  $\gamma$  for  $i = 10^\circ$  (Model A: solid),  $60^\circ$  (Model B: dotted) and  $80^\circ$  (Model C: dashed) from left to right respectively. All the profiles are computed at the rotational phase of  $0.75$  (c.f. Fig. 6). Overall dependency on the inclination angles are similar for all three transitions although the relative strength slightly decreases from H to Pa then to Br. The line cores are narrower for higher inclination angle models. The strength of the blue wings are similar for  $i = 10^\circ$  and  $60^\circ$ , but much weaker in the higher inclination model  $i = 80^\circ$  since the most of the flow moving toward an observer (blueshifted flows) is eclipsed by the stellar surface in a higher inclination (c.f. Fig. 6). The depth of the red wing absorption is largest for  $i = 60^\circ$  cases where the alignment of a hot spot–infall stream–observer is near optimum.

second hot spot (c.f. Section 3.1) from the lower hemisphere at this rotational phase causes a slight increase in the continuum flux as also seen in the light curve in Fig. 4. This slightly weakens the line strength even further.

For larger misalignment models (Models D and E), we observe two local minima in one rotational period. As mentioned earlier, the two local minima are seen because of the visibility of two hot spots in these models at this inclination ( $i = 60^\circ$ ). Remember that the continuum light curves of these models (Fig. 4) also show two local minima in one rotational phase. We note that the position of the local minima in the EW for these two models coincide well with the position of the maxima (or local maxima) of the continuum light curves in Fig. 4. This clearly demonstrates that the hot spot visibility greatly influences the line EW variability. To quantify the statement above, we have computed the Pearson’s correlation coefficients ( $r$ , c.f. Bevington 1969) for the continuum light curves in Fig. 4 and the EW curves in Fig. 13 for each model. The results are  $r = 0.67, 0.92, 0.95, 0.88, 0.99$  for Models A, B, C, D and E respectively — indicating fairly good correlations between the continuum and the EW variations.

The EW of the red wing and that of the blue wing of each model are well correlated with each other except for Model C which has a very high inclination ( $i = 80^\circ$ ). The figure shows that during half of the rotational period (between  $\tau = 0$  and  $0.5$ ), the EW curves are anti-correlated each other. This anti-correlation is naturally caused by the fact that only one accretion arm is visible to an observer at this high inclination. When the arm is on the opposite side of the star (when the star is in between the observer and the arm), the EW of the blue wing should be maximum and that of the red wing should be minimum. When the arm is on near side of the observer, the opposite should occur if the hot spots are not visible to the observer. As explained earlier, the high visibility of the hot spot on the upper hemisphere causes the increase in the continuum flux resulting in lower EW in the red wing for the phase between  $\tau = 0.5$  and  $1.0$ , causing the correlation between the EW of the red wing and the blue wing (instead of an anti-correlation).

In the time-series spectra observation of the CTTS SU Aur,

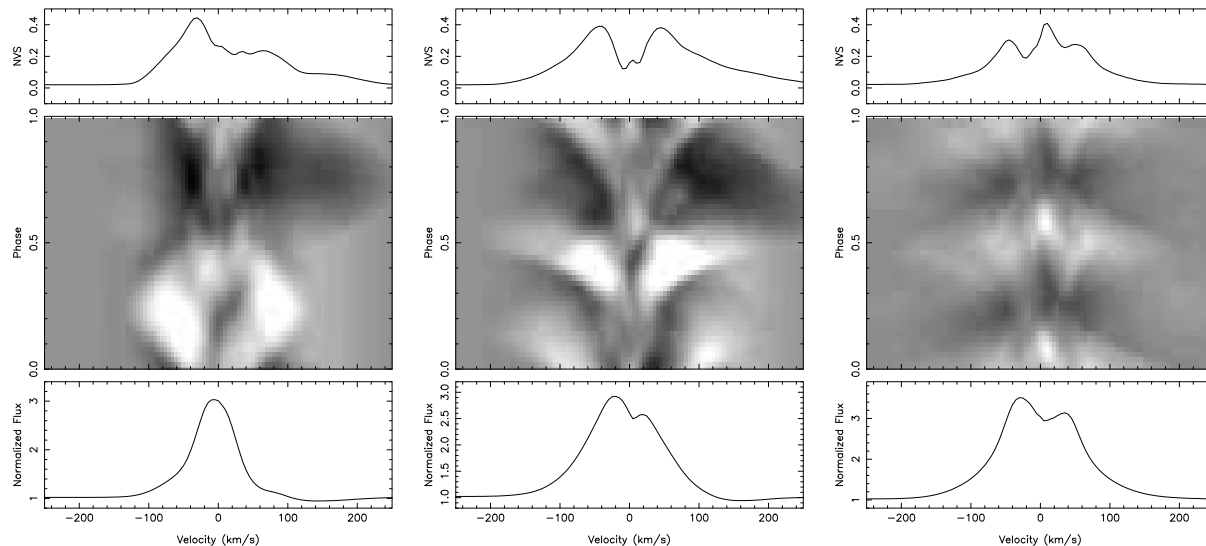


**Figure 10.** Same as in Fig. 8, but for different magnetic misalignment angles:  $\theta = 15^\circ$  (left, Model B),  $60^\circ$  (centre, Model D), and  $90^\circ$  (right, Model E). The inclination is fixed at  $i = 60^\circ$  for these models. The mean spectrum (bottom panels) becomes wider and more asymmetric (around the line centres) as  $\theta$  increases. A weak absorption in the red wing are seen in the mean spectra for  $\theta = 15^\circ$  and  $60^\circ$  cases, but no clear red absorption is seen in  $\theta = 90^\circ$  case. The variability patterns (middle and top panels) for three cases are quite distinct from one another.

Johns & Basri (1995) found an anti-correlation between the blue wing EW of H $\beta$  and the red wing EW of H $\gamma$ . They discussed that the anti-correlation might be explained by a tilted dipole magnetosphere with outflow components from the disc-magnetosphere interaction region. Although there is no wind/outflow component in our model, the mechanism producing the anti-correlation seen in Model C may be also an additional reason for the observed anti-correlation in SU Aur. We also note that the high inclination which is required for this mechanism is consistent with the high inclination angle of SU Aur (e.g. Muzerolle et al. 2003; Unruh 2004; Kurosawa et al. 2005). In time-series spectroscopic observation of Pa $\beta$  from SU Aur, Kurosawa et al. (2005) also found the EW of the red wing anti-correlates with that of the blue wing at some rotational phases, but they correlate in other phases. Once again this behaviour is quite similar to that one seen our Model C.

## 4 DISCUSSION

### 4.1 Comparison with observations

Although not based on simultaneous observations, Folha & Emerson (2001) presented 42 Pa $\beta$  and 30 Br $\gamma$  profiles of CTTS and weak T Tauri stars (WTTS) mainly in the Taurus-Auriga complex. They found that 53 per cent of Pa $\beta$  profiles have shapes symmetric around the line centre (Type I profile: Reipurth et al. 1996) and 34 per cent of them have IPC profiles. Similarly for Br $\gamma$ , they found 72 and 20 per cent for Type I and IPC profiles respectively. They also found no blueshifted absorption components in both Pa $\beta$  and Br $\gamma$  except in one object (CW Tau) and only in Pa $\beta$ .

All of our models in Figs. 6 and 7 (except for Model E) show the IPC at some rotational phases. For Br $\gamma$ , in general we found that the IPC feature (the redshifted absorption component) is much weaker than that seen in the Pa $\beta$ . For example, Fig. 11 shows the flux level in the red wing remains above the continuum for mid to low inclination systems, and it is below the continuum level only

for a very high inclination system. Using the time-series model spectra (which are equally sampled in rotational phase) shown in Figs. 8, 10 and 12, we have computed the fraction of the occurrence of IPC profiles in each model. The results are summarised in Table 3 along with the fraction of the IPC profiles in the Pa $\beta$  and Br $\gamma$  from the observations of Folha & Emerson (2001). For a fixed  $i$  value (Models A, B and C), the fraction of the IPC profiles decreases as the inclination angle  $i$  increases for Pa $\beta$ . The largest inclination model ( $i = 80^\circ$ , Model C) shows the fraction of IPC profiles is 37 per cent which is closest to the observed value of 34 per cent. On the other hand, no such clear trend is seen for the Pa $\beta$  models with the fixed  $i = 60^\circ$  value but for different  $\theta$  values (i.e. Models B, D and E). At this mid-inclination angle  $i = 60^\circ$  ( $\cos i = 0.5$ ), the fraction of IPC profiles (for Pa $\beta$ ) is 50, 50 and 0 per cent for Models B, D and E respectively. The fractions for Models B and D are much larger than that of the observations, and that for Model E is much smaller. To compare the models more strictly with the IPC fractions of the observations, one needs enough sampling of the model profiles in both rotational phase and inclination angle. Although we have enough phase sampling points (50 angles), we lack a full sampling of inclination angle (3 angles); hence, the direct comparison is difficult here.

The full width half maxima (FWHM) of the mean (phase-averaged) Pa $\beta$  and Br $\gamma$  spectra of our models (Figs. 8, 10 and 12) are also summarised in Table 3 along with the mean FWHM of the observed Pa $\beta$  and Br $\gamma$  profiles from Folha & Emerson (2001). The table clearly shows that in all models presented here, the predicted FWHM underestimate the observed values. The discrepancy may be caused by one or a combination of the following: (1) the relatively small size of the magnetosphere in the MHD models in which the gas velocities just before reaching the stellar surface is relatively small  $\sim 200 \text{ km s}^{-1}$ , (2) the spatial widths of the accretion funnels are underestimated, (3) other line broadening mechanisms (besides the Doppler) may be important (e.g. Muzerolle et al. 2001; Kurosawa et al. 2006), and (4) the temperature of funnel streams is underestimated. An implication for possible cause (2) can be seen in the tendency of increasing FWHM values as increasing  $i$  val-

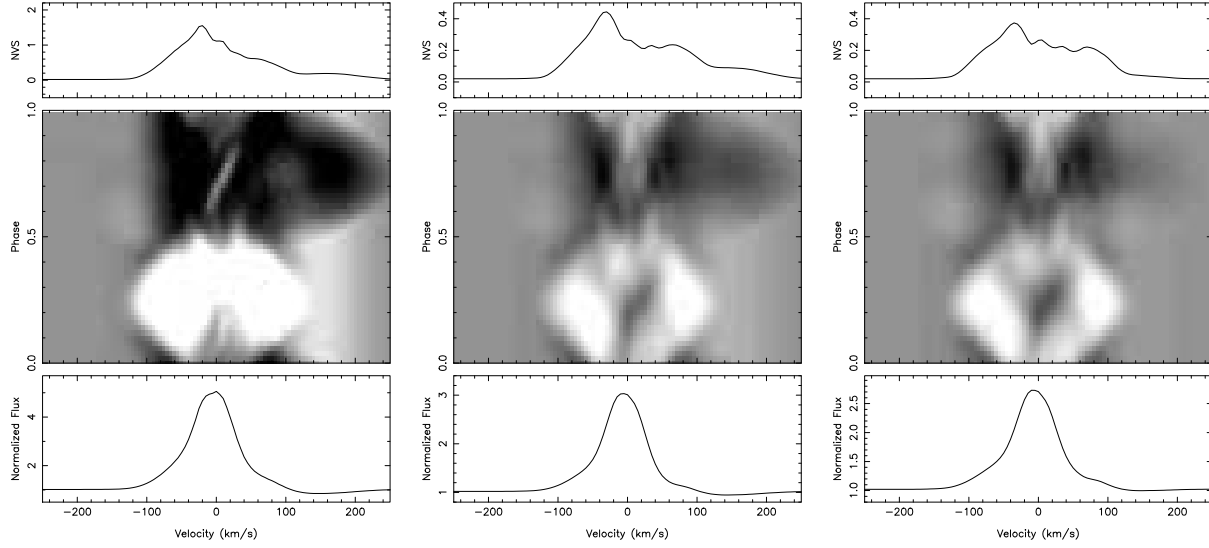


**Figure 12.** Same as in Fig. 8, but for Models B ( $i = 60^\circ$  and  $\alpha = 15^\circ$ ) with different lines: H (left), Pa (centre) and Br (right). The line strength of the mean spectra (bottom panels) decreases from H to Pa, and then to Br. All lines show a similar variability pattern as seen in their quotient spectra greyscale images (middle panels); however, they differ in their magnitudes (top panels).

ues. Note that the widths of the accretion streams become wider for a larger  $\alpha$  model. As mentioned before (Section 2.3), the normalisation of the temperature structures used in our models is quite arbitrary, and the temperatures used here may underestimate that of a typical CTTS.

We also find that among our models only  $\alpha = 15^\circ$  models (Models A, B and C) show rather symmetric Type I profiles. The larger  $\alpha$  models (Models D and E) show profiles split near the line centres, and have an appearance of a double-peaked profile. The difference is mainly caused by the geometry of the accretion funnels and the locations of the hot spots where the accretion funnels meet the stellar surface. In Models D and E with  $\alpha = 60^\circ$  and  $90^\circ$  respectively, the accretion funnels are much wider and the hot spot latitudes are much lower compared to those of the  $\alpha = 15^\circ$  models. This would allow an observer to see near the base of the accretion funnels from both hemisphere for the larger misalignment angle models (c.f. Fig. 7). This and the rotational motion of the magnetosphere causes a double-peaked profiles. On the other hand, in the low misalignment angle models, the base of only one accretion funnel is visible to an observer (c.f. Fig. 6). Based on the comparison of the line profile shapes, we find that a model with a smaller misalignment angle ( $\alpha = 15^\circ$ ) is more consistent with the observations of Folha & Emerson (2001). Note that the double-peaked profile shapes (Type II-R, c.f. Reipurth et al. 1996) seen in Models D and E are not entirely inconsistent with the observations, as Folha & Emerson (2001) found such Pa profiles in a few systems.

The hot spot surface coverage fractions in our models (in Figs. 6 and 7) are approximately 7 per cent (for Models A, B and C), 9 per cent (for Model D) and 6 per cent (for Model E). These values seem rather large compared to the hot spot coverage indicated by observations. For example, Calvet & Gullbring (1998) found that for the majority of CTTS, the filling factor is  $f = 0.001 - 0.01$ , and the corresponding surface coverage of the spots is only 0.1–1 per cent of the stellar surface (see also Gullbring et al. 2000). Indeed, these sizes are in agreement with those derived by Valenti, Basri, & Johns (1993) using spectrophotometric observations of ‘blue continuum.’ However, Muzerolle et al. (1998b)

Model/Obs.	FWHM ( $\text{km s}^{-1}$ )		IPC fraction (per cent)
Observation (Pa )	204	12	34
Model A (Pa )	42		100
Model B (Pa )	70		50
Model C (Pa )	70		37
Model D (Pa )	113		50
Model E (Pa )	129		0
Observation (Br )	207	26	20
Model B (Br )	70		31

**Table 3.** Comparison with the observation of Folha & Emerson (2001). See Table 2 for model parameters.

pointed out that the filling factor  $f$  seems to be much larger at longer wavelengths, and it was suggested that possibly the filling factor depends on wavelength. Here we note that the hot spots obtained in the 3-D MHD simulations are strongly inhomogeneous i.e. the kinetic energy per unit area (matter flux) is much larger in the centre of the spot compared to peripheral regions of the spot (c.f. see Figs. 2 and 3 in Romanova et al. 2004).

In addition, the line strength and shape of the models are not expected to be very sensitive to a hot spot coverage, provided that the mass-accretion rate and hence the hot spot luminosity is unaffected by the change in the size of hot spot itself. However, if the hot spot coverage becomes much larger (e.g. 30 per cent), then the geometry of the magnetosphere itself must change significantly. This would result in a significant change in the line shapes. In general, the lines are more sensitive to mass-accretion rates and consequently to hot spot luminosities. A possible effect of a reduced hot spot coverage area in the model would be a smaller chance of producing the IPC profiles. In turn, this would give us a better agreement with the IPC fraction seen in the observations of Folha & Emerson (2001), as discussed earlier (c.f. Table 3).

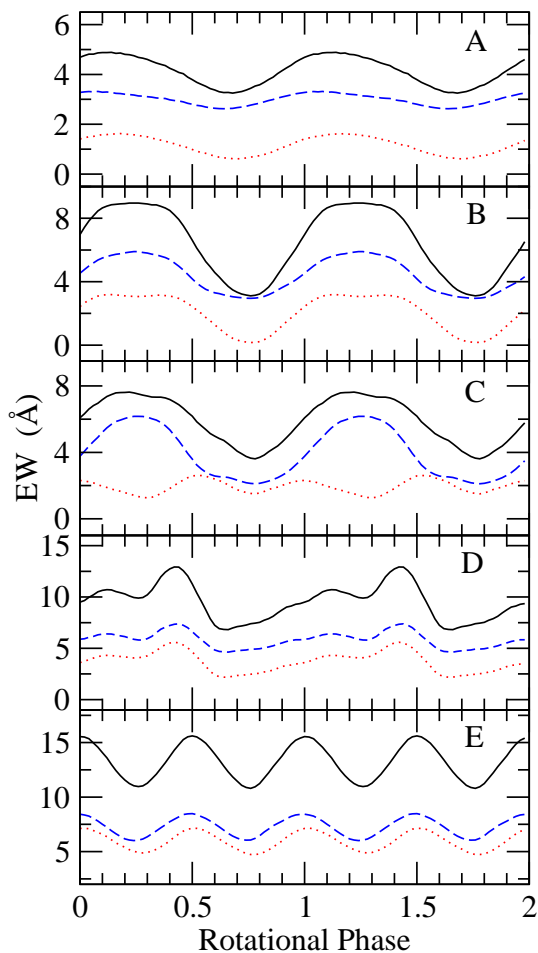


**Figure 13.** Equivalent width (EW) variations as a function of rotational phase for the six models (A through F) in Table 2. For each model, the total EW (solid), the EW in the red wing (dotted), and that in the blue wing (dashed) are separately computed. Except for Model C, the temporal variations of the EW in the red wing and that in the blue wing are well correlated. For Model C, they are anti-correlated between phase  $\tau = 0$  and  $0.5$  (see text for explanation).

## 4.2 Intrinsic variability

In the previous section (Section 3), we presented the ‘rotationally modulated’ variability of the spectra based on the MHD simulations. We observed that the variability associated with the absorption in the red wing reaches up to 30–40 per cent (c.f. Figs. 8, 10 and 12). Here we briefly examine whether such rotationally modulated variability can be observed when, in reality, the accretion rate through the funnels to the stellar surface may also vary in time. The MHD simulations have shown that in many cases the mass-accretion rate ( $\dot{M}_-$ ) to the stellar surface reaches quasi-stationary states, but the mass flux continues to vary on a time-scale of 3–5 d, which is similar to the rotationally modulated time-scale ( $\approx 4$  d). Thus the line profile variability induced by the stellar rotation may be complicated by the intrinsic variation of the accretion rate. However, the MHD simulations show that in one of the main cases ( $\beta = 15$  and  $\alpha = 1.1$ ), the accretion rate  $\dot{M}_-$  is almost constant, and varies only at the level of 5–6 per cent. In this case, we expect that the effect of the intrinsic variability on the line variability is relatively small, and the results presented in the previous section are not affected significantly. On the other hand, in case for

$\beta = 15$  and  $\alpha = 5/3$  (c.f. Romanova et al. 2003, 2004), we find that the variation of  $\dot{M}_-$  occurs at the level of 10–30 per cent. We expect in this case, the line profile variability to be affected by the change in  $\dot{M}_-$ , which occurs on a similar time scale as the rotational period but varies rather stochastically. The line variability will be a mixture of periodic signals from stellar rotation and rather random signals from the change in  $\dot{M}_-$ . However, we expect that in this case long simulation runs will help to separate the contribution from this large but random component (caused by the change in  $\dot{M}_-$ ) from the total line variability.

## 4.3 The Sobolev approximation

Although not explicitly shown here, the funnel flow velocities near the inner edge of the accretion disc are rather slow and subsonic. For example in Models A, B, and C ( $\beta = 15$  cases), the flow velocities are very similar to the one shown in Fig. 5 (right panel) of Romanova et al. (2004) in which the Mach number of the gas flow in the middle of the funnel flow is plotted as a function of distance from the star (along the stream line). The plot shows that most of the flow is in fact supersonic except for the gas near the disc. The Sobolev Approximation used in the radiative transfer models is not quite valid in the subsonic part of the flow; however, most of the line emission occurs in the funnel flow near the stellar surface (c.f. Figs. 6 and 7), and the line of sight to the emission region does not pass through the slow moving part of the funnel flow near the inner edge of accretion disc, except for a very high inclination case. For this reason, the Sobolev approximation used in the line profile models presented here should be a reasonable assumption, provided that the intrinsic line width is negligible compared to the Doppler broadening due to the bulk (macroscopic) motion of gas.

In Section 4.1, we noted that the possibility of additional line broadening mechanisms besides the the Doppler may be important for explaining much larger FWHMs seen in the observed Pa  $\gamma$ , compared to those from our models. Muzerolle et al. (2001) and Kurosawa et al. (2006) considered Stark broadening which is important in optically thick lines e.g. H  $\gamma$ , but less likely important for Pa  $\gamma$  and Br  $\gamma$  lines. Another possible cause of line broadening is due to large turbulent motion of plasma which could be caused by Alfvén waves excited in the magnetosphere (c.f. Johns & Basri 1995). If the magnitude of turbulent velocity is comparable to that of the local thermal velocity, the assumption of the Sobolev approximation becomes invalid. The MHD simulations presented in this paper do not show such turbulent motions; hence, we have simply adopted the Sobolev approximation in the work presented here. On the other hand, if large turbulence is found in the MHD simulations, the radiative transfer models should abandon the Sobolev approximation and used an alternative method e.g. the ray-by-ray integration method in Muzerolle et al. (2001) and Kurosawa et al. (2006).

## 4.4 Comparison with earlier models

Although very successful in explaining many CTTS emission line features, the MA model of Muzerolle et al. (2001) are axisymmetric (2.5-D); hence, they cannot predict the line variability associated with stellar rotation. On the other hand, their model still can predict line variability caused by a non-constant mass-accretion rate. Kurosawa et al. (2006) introduced the disc wind – MA hybrid model by combining the models of Knigge, Woods & Drew (1995) and Hartmann et al. (1994) i.e. including both outflows and inflows



from and to the CTTS. The model was successful in reproducing the wide variety of H $\alpha$  profile shapes seen in observations, and it demonstrated the importance of a wind or outflow component in determining the profiles shapes of H $\alpha$ . Their models were also axisymmetric, and did not consider line variability.

The same dipole MA model as in Hartmann et al. (1994) and Muzerolle et al. (2001) are used in the 3-D Monte Carlo radiative transfer model of Symington et al. (2005a) (see also Kurosawa et al. 2005). They have modified the magnetosphere by removing the flow within some azimuthal angle ranges, and then displaced the magnetic poles from the rotational poles to imitate the flow geometry found in the MHD simulation of R03 and R04, to simulate a possible line variability for  $i = 60^\circ$  case. The misalignment angle used in this model (their A30 model) is rather small ( $10^\circ$ ), and it is very similar to our  $i = 15^\circ$  models. Although the line strength is much weaker than our Model B (which also uses  $i = 60^\circ$ ), the variability pattern seen in their RMS spectra and the quotient spectra image (see their Figure 9) are very similar to ours (Fig. 8). The difference in the line strength is caused by the difference in the adopted mass-accretion rate and the mass-weighted mean temperature between the two models.

## 5 CONCLUSIONS

We have presented a series of 3-D Monte Carlo radiative transfer calculations of the line variability from CTTS induced by stellar rotation using the results of the 3-D MHD simulations of Romanova et al. (2003, 2004) who considered the accretion onto the CTTS with a misaligned dipole axis with respect to the rotational axis. Our model here does not include an outflow component, and is restricted to the case of accretion flow through the magnetosphere. Main objectives here were firstly to examine whether the 3-D MHD simulations would be able to reproduce the types of line profiles and the line variability seen in observations, and secondly to examine how the line variability depends on basic physical parameters. In the following, we will summarise our main findings though this investigation.

(1) The detail of the temperature structure along the accretion funnel flow does not affect the line shapes greatly (Section 3.2). For a fixed (density-weighted) mean temperature ( $T_{\text{mean}}$ ) of the accretion flow, we have considered three different temperature structures (HCH, ACH and isothermal c.f. Section 2.3), and found the resulting Pa $\gamma$  profiles are very similar to each other, at least with  $T_{\text{mean}} = 8000\text{ K}$ . The line shapes are more sensitive to the inclination of the systems, the geometry and hence the velocity field of the accretion flow.

(2) By comparing our models with the atlas of observed Pa $\gamma$  and Br $\gamma$  profiles of Folha & Emerson (2001), we found models with a smaller misalignment angle (e.g.  $i = 15^\circ$ ) produce rather symmetric profiles which are seen in the majority of the observed sample. The models with mid to high misalignment angles produces double-peaked profiles (Type II-R: Reipurth et al. 1996) which are very rare in the sample of Folha & Emerson (2001). This may also suggest that the majority of the CTTS have a rather small misalignment angle.

(3) We find that the line equivalent width variability is closely related with the visibility of the hot spots on the stellar surface (Section 3.6). For a high inclination system with a small dipole misalignment angle (e.g. Model C), only one accretion of funnel (on the upper hemisphere) is visible to an observer at any given rotational phase; hence, the anti-correlation of the EW in the blue wing

and that in the red wing can occur during half of a rotational period, specifically when the hot spot is not visible to the observer (Fig. 13).

(4) Based on our line profile models, we find that the MHD models of Romanova et al. (2003, 2004) are capable of reproducing line profile variability behaviour similar to those seen in observations (e.g. Alencar & Batalha 2002; Kurosawa et al. 2005; Bouvier et al. 2007b) although the original temperature predicted by the MHD models had to be lowered by an arbitrary scaling factor in the radiative transfer calculation due to lack of a proper cooling mechanism in the MHD model (c.f. Sections 2.3).

Despite of the relatively good agreement between our models and observed line variability, several issues still remain. First, the assumption of the Sobolev approximation used in the radiative transfer calculation may not be valid in the funnel flow near the inner edge of the accretion disc where the speed of flow is substantially subsonic. Relaxing this assumption may be more important in the observed flux calculation than in the source function calculation according to the finding of Bastian et al. (1980) who compared line profiles computed in 1-D (spherical geometry), using three different radiative transfer methods including the Sobolev approximation method. Detailed investigation of the validity of the Sobolev approximation in the context of the magnetospheric accretion is underway, and shall be presented in a future paper (Harries et al., in preparation).

Second, the model presented here does not include a wind component. Although the effect of the wind on the line profile shapes are expected to be small in Pa $\gamma$  and Br $\gamma$ , it could potentially have significant effects on H $\alpha$  and H $\beta$  (e.g., Reipurth et al. 1996; Alencar & Basri 2000). Strong wind absorption components are also seen the optically thick He I 10830 line (Edwards et al. 2003; Dupree et al. 2005; Edwards et al. 2006). These spectroscopic observations combined with models (e.g., Matt & Pudritz 2005, 2007; Ferreira, Dougados & Cabrit 2006; Kurosawa et al. 2006; Kwan, Edwards & Fischer 2007) provide us with opportunities to constrain little known physical properties (e.g. geometry and temperature) of the wind/outflow in sub-AU scales. However, as the MHD models used in this paper do not include the outflow, we are not be able to explore the possible effect of the wind contribution to line variability. In principle, our radiative transfer model can be applied to a system which includes both the MA flow and the wind once a result of such MHD calculations becomes available.

Strict tests of our models should be performed by quantitative fitting of the time-series observations of multiple lines (e.g., Johns & Basri 1995; Unruh 2004; Bouvier et al. 2007b) with good rotational phase coverages. The different lines are formed in different volumes within the funnels and give us additional information on the flow kinematics. The spectra from different rotational phases provides information on how the magnetosphere changes in azimuthal direction. Once the validity of the model is established, it can be used to constrain the complex geometry of the MA flows around CTTS. It would be very interesting to compare the geometry constrained by this method to the ones determined from the field extrapolation method (e.g. Jardine, Collier Cameron & Donati 2002; Gregory et al. 2006) using the stellar surface magnetic field information via the Zeeman-Doppler imaging technique, obtained with a modern stellar spectropolarimeter such as ESPaDOnS (Donati et al. 2006; Donati et al. 2007).

While our underlying assumption of the magnetic field geometry is pure dipole, a more complex field geometry, such as in Long et al. (2007) who considered the combination of a dipole and a quadrupole fields in their MHD models, should be also considered

in the line variability calculations. For example, some CTTS are known to possess non-dipole magnetic fields (c.f. Johns-Krull et al. 1999; Valenti & Johns-Krull 2004; Donati et al. 2007). Finally, we shall also consider the case with a non-constant mass-accretion rate model. For example, a recent MHD calculation by Kulkarni & Romanova in preparation (see Romanova et al. 2007) has shown that variable mass-accretion rates could occur due to instabilities (Rayleigh-Taylor and Kelvin-Helmholtz) in the MA flow. These add another level of complexity in the interpretation of observed line profiles, and their variability.

## ACKNOWLEDGEMENTS

We thank the referee, Dr. Chris Johns-Krull, who provided us with valuable comments and suggestions which improved the clarity of the manuscript. This work is partially supported by PPARC rolling grant PP/C501609/1, and benefited from a research visit by RK funded by Exeter's visitors grant PP/D001617/1. This work was also supported in part by NASA grants NAG5-13220, NAG5-13060, and by NSF grant AST-0307817, AST-0507760 and AST-0607135. This work was also supported by NASA through grant HST-AR-10680 from the Space Telescope Science Institute, which is operated by the Association of Universities for Research in Astronomy, Inc., under NASA contract NAS5-26555. The numerical computations presented in this paper were performed partly on the NASA computing facilities, specifically Explore and Columbia. RK thanks Prof. Richard Lovelace for his hospitality during a visit at Cornell University. RK is grateful for Dr. Daniel Proga for helpful discussions and enthusiastic support for this work, and is also grateful for Dr. Neil H. Symington for his effort in the development of crucial parts of the code TORUS.

## REFERENCES

- Alencar S. H. P., Basri G., 2000, *AJ*, 119, 1881  
 Alencar S. H. P., Batalha C., 2002, *ApJ*, 571, 378  
 Bastian U., Bertout C., Stenholm L., Wehrse R., 1980, *A&A*, 86, 105  
 Bevington P. R., 1969, *Data reduction and error analysis for the physical sciences*. McGraw-Hill, New York  
 Bouvier J., Alencar S. H. P., Harries T. J., Johns-Krull C. M., Romanova M. M., 2007a, in Reipurth B., Jewitt D., Keil K., eds, *Protostars and Planets*. University of Arizona Press, Tucson, p. 479  
 Bouvier J. et al., 2007b, *A&A*, 463, 1017  
 Calvet N., Gullbring E., 1998, *ApJ*, 509, 802  
 Calvet N., Muzerolle J., Briceño C., Hernández J., Hartmann L., Saucedo J. L., Gordon K. D., 2004, *AJ*, 128, 1294  
 Camenzind M., 1990, in Klare G., ed., *Reviews in Modern Astronomy Vol. 3, Magnetized Disk-Winds and the Origin of Bipolar Outflows*. Springer, Berlin, p. 234  
 Donati J.-F., Forveille T., Cameron A. C., Barnes J. R., Delfosse X., Jardine M. M., Valenti J. A., 2006, *Science*, 311, 633  
 Donati et al., 2007, *MNRAS*, 380, 1297  
 Dupree A. K., Brickhouse N. S., Smith G. H., Strader J., 2005, *ApJ*, 625, L131  
 Edwards S., Fischer W., Hillenbrand L., Kwan J., 2006, *ApJ*, 646, 319  
 Edwards S., Fischer W., Kwan J., Hillenbrand L., Dupree A. K., 2003, *ApJ*, 599, L41  
 Edwards S., Hartigan P., Ghandour L., Andrulis C., 1994, *AJ*, 108, 1056  
 Ferreira J., Dougados C., Cabrit S., 2006, *A&A*, 453, 785  
 Folha D. F. M., Emerson J. P., 2001, *A&A*, 365, 90  
 Fullerton A. W., Gies D. R., Bolton C. T., 1996, *ApJS*, 103, 475  
 Gregory S. G., Jardine M., Simpson I., Donati J.-F., 2006, *MNRAS*, 371, 999  
 Gullbring E., Calvet N., Muzerolle J., Hartmann L., 2000, *ApJ*, 544, 927  
 Gullbring E., Hartmann L., Briceno C., Calvet N., 1998, *ApJ*, 492, 323  
 Harries T. J., 2000, *MNRAS*, 315, 722  
 Hartmann L., Avrett E., Edwards S., 1982, *ApJ*, 261, 279  
 Hartmann L., Calvet N., Gullbring E., D'Alessio P., 1998, *ApJ*, 495, 385  
 Hartmann L., Hewett R., Calvet N., 1994, *ApJ*, 426, 669  
 Herbst W., Bailer-Jones C. A. L., Mundt R., Meisenheimer K., Wackermann R., 2002, *A&A*, 396, 513  
 Hillier D. J., 1991, *A&A*, 247, 455  
 Jardine M., Collier Cameron A., Donati J.-F., 2002, *MNRAS*, 333, 339  
 Johns C. M., Basri G., 1995, *AJ*, 109, 2800  
 Johns C. M., Basri G., 1995, *ApJ*, 449, 341  
 Johns-Krull C. M., 2007, *ApJ*, 664, 975  
 Johns-Krull C. M., Valenti J. A., Hatzes A. P., Kanaan A., 1999, *ApJ*, 510, L41  
 Klein R. I., Castor J. I., 1978, *ApJ*, 220, 902  
 Knigge C., Woods J. A., Drew J. E., 1995, *MNRAS*, 273, 225  
 Koenigl A., 1991, *ApJ*, 370, L39  
 Koldoba A. V., Romanova M. M., Ustyugova G. V., Lovelace R. V. E., 2002, *ApJ*, 576, L53  
 Kulkarni A. K., Romanova M. M., 2005, *ApJ*, 633, 349  
 Kurosawa R., Harries T. J., Bate M. R., Symington N. H., 2004, *MNRAS*, 351, 1134  
 Kurosawa R., Harries T. J., Symington N. H., 2005, *MNRAS*, 358, 671  
 Kurosawa R., Harries T. J., Symington N. H., 2006, *MNRAS*, 370, 580  
 Kurucz R. L., 1979, *ApJS*, 40, 1  
 Kwan J., Edwards S., Fischer W., 2007, *ApJ*, 657, 897  
 Long M., Romanova M. M., Lovelace R. V. E., 2005, *ApJ*, 634, 1214  
 Long M., Romanova M. M., Lovelace R. V. E., 2007, *MNRAS*, 374, 436  
 Martin S. C., 1996, *ApJ*, 470, 537  
 Matt S., Pudritz R. E., 2005, *ApJ*, 632, L135  
 Matt S., Pudritz R. E., 2007, preprint (astro-ph/0707.0306)  
 Muzerolle J., Calvet N., Hartmann L., 1998a, *ApJ*, 492, 743  
 Muzerolle J., Calvet N., Hartmann L., 2001, *ApJ*, 550, 944  
 Muzerolle J., Calvet N., Hartmann L., D'Alessio P., 2003, *ApJ*, 597, L149  
 Muzerolle J., Hartmann L., Calvet N., 1998b, *AJ*, 116, 455  
 Reipurth B., Pedrosa A., Lago M. T. V. T., 1996, *A&AS*, 120, 229  
 Romanova M. M., Kulkarni A. K., Lovelace R. V. E., 2007 (astro-ph/0711.0418)  
 Romanova M. M., Ustyugova G. V., Koldoba A. V., Lovelace R. V. E., 2002, *ApJ*, 578, 420 (R02)  
 Romanova M. M., Ustyugova G. V., Koldoba A. V., Lovelace R. V. E., 2004, *ApJ*, 610, 920 (R04)  
 Romanova M. M., Ustyugova G. V., Koldoba A. V., Wick J. V., Lovelace R. V. E., 2003, *ApJ*, 595, 1009 (R03)  
 Rybicki G. B., Hummer D. G., 1978, *ApJ*, 219, 654

- Symington N. H., Harries T. J., Kurosawa R., 2005a, MNRAS, 356, 1489
- Symington N. H., Harries T. J., Kurosawa R., Naylor T., 2005b, MNRAS, 358, 977
- Unruh Y. C. et al., 2004, MNRAS, 348, 1301
- Ustyugova G. V., Koldoba A. V., Romanova M. M., Chechetkin V. M., Lovelace R. V. E., 1999, ApJ, 516, 221
- Ustyugova G. V., Koldoba A. V., Romanova M. M., Lovelace R. V. E., 2006, ApJ, 646, 304
- Valenti J. A., Basri G., Johns C. M., 1993, AJ, 106, 2024
- Valenti J. A., Johns-Krull C. M., 2004, Ap&SS, 292, 619